









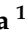




## Article

# Cobalt Doping Effects in Zinc Oxide: A Combined Experimental and Ab Initio Approach

Luciano F. D. Pereira <sup>1,\*</sup> , Wanderson L. Ferreira <sup>1</sup> , Bruno S. Correa <sup>1</sup> , Messias S. Costa <sup>2</sup> , Cleidilane S. Costa <sup>2</sup> , Arnaldo A. M. Filho <sup>1</sup> , Tatiane S. N. Sales <sup>1</sup> , Brianna Bosch-Santos <sup>1</sup> , Juliana Schell <sup>3,4</sup> , Anastasia Burimova <sup>1</sup> , Rajendra N. Saxena <sup>1</sup> , Gabriel A. Cabrera-Pasca <sup>2,5</sup>  and Artur W. Carbonari <sup>1,\*</sup> 

- <sup>1</sup> Instituto de Pesquisas Energéticas e Nucleares IPEN-CNEN/SP, São Paulo 05508-000, Brazil; wlferreira@usp.br (W.L.F.); bruno27ni@gmail.com (B.S.C.); arnaldoalves26@gmail.com (A.A.M.F.); tatianenas1@gmail.com (T.S.N.S.); briannabs@yahoo.com.br (B.B.-S.); anstburimova@gmail.com (A.B.); rnsaxena@ipen.br (R.N.S.)
- <sup>2</sup> Campus de Abaetetuba, Universidade Federal do Pará, Abaetetuba 68440-000, Brazil; mscosta@ufpa.br (M.S.C.); cleidilane@ufpa.br (C.S.C.); gpasca@ufpa.br (G.A.C.-P.)
- <sup>3</sup> European Organization for Nuclear Research (CERN), CH-1211 Geneva, Switzerland; juliana.schell@cern.ch
- <sup>4</sup> Institute for Materials Science and Center for Nanointegration Duisburg-Essen (CENIDE), University of Duisburg-Essen, 45141 Essen, Germany
- <sup>5</sup> Programa de Pós-Graduação em Ciência e Engenharia de Materiais-PPGCEM, Universidade Federal do Pará-UFGPA, Ananindeua 67130-660, Brazil
- \* Correspondence: lucianofabricio@gmail.com (L.F.D.P.); carbonar@ipen.br (A.W.C)

**Abstract:** In this paper, we investigate the solubility effects of Co in ZnO ( $Zn_{1-x}Co_xO$ , where  $x = 0, 0.03, 0.05, 0.1, 0.2, 0.25, 0.4, 0.8,$  and  $1$ ) by combining the results of perturbed angular correlation (PAC) spectroscopy using highly diluted  $^{111}Cd$  as probe nuclei and ab initio calculations based on spin-density functional theory (SDFT). This combined approach enables us to characterize the local structure around Cd ions, where, through PAC technique, it was possible to measure the EFG as a function of temperature and Co concentration and thereby monitor the changes in the structure and the Co solubility threshold in ZnO and the ZnO/CoO/Co<sub>3</sub>O<sub>4</sub> mixed phase. The full-potential linear augmented plane wave plus local orbital (APW+lo) formalism were used here to describe the electronic structure of the supercells, including the atomic relaxations. These Ab initio calculations show an interesting behavior of the Cd and Co impurity levels in the band structure of ZnO, which explains the experimental results in terms of the origin of EFG and the evidence of ferromagnetic response.

**Keywords:** ZnO; Co doping; solubility behavior; electric field gradient; perturbed angular correlations; Ab initio calculations; nuclear solid-state physics



**Citation:** Pereira, L.F.D.; Ferreira, W.L.; Correa, B.S.; Costa, M.S.; Costa, C.S.; Filho, A.A.M.; Sales, T.S.N.; Bosch-Santos, B.; Schell, J.; Burimova, A.; et al. Cobalt Doping Effects in Zinc Oxide: A Combined Experimental and Ab Initio Approach. *Crystals* **2024**, *14*, 51. <https://doi.org/10.3390/cryst14010051>

Academic Editor: Claudio Cazorla

Received: 9 November 2023

Revised: 15 December 2023

Accepted: 22 December 2023

Published: 29 December 2023



**Copyright:** © 2023 by the authors. Licensee MDPI, Basel, Switzerland. This article is an open access article distributed under the terms and conditions of the Creative Commons Attribution (CC BY) license (<https://creativecommons.org/licenses/by/4.0/>).

## 1. Introduction

The technological and commercial importance of transition metal oxides (TMOs) has grown in recent years [1–3]. The dissolution of transition metals (e.g., TM = Zn, Ni, Cu, Ti) in a semiconductor matrix allows for the control of charge carriers, vacancies, and lattice distortions, as well as magnetic behavior and optical gap changes. These properties can enable advanced capabilities for materials in applications such as spintronics and magneto-optics [4–6]. Another promising capability in semiconductors is the solid solution (doping or alloying), which has proven to be efficient and useful, because it allows for the control of band gaps in these materials [7].

On the other hand, the occurrence of magnetism in semiconductors is a subject of intensive discussion in the literature, which may be associated with the following situations: (i) The nanometer-scale size reduction due to surface/volume effects brings a spin decompensation at the surface, thereby inducing magnetism in these semiconductor materials [8,9]; (ii) Magnetic coupling can also be turned on by the dilution of transition

metal-3d (TM-3d types) or rare-earth-4f (RE-4f types), which are called diluted magnetic semiconductors (DMSs), where long-range spin–spin interaction is a key factor [4]. (iii) The magnetism arising from solid solutions has been studied intensively in the last decades, since this mechanism allows for tuning the magnetism and band gaps in semiconductor materials. The process of atomic dilution or the solid solution in semiconductor matrices may involve different scenarios such as the following: the substitution of atoms (TM) in the lattice, the location of the TM atoms in the lattice interstitial, the formation of clusters, or the phase separation [10]. The control of these possible scenarios requires the ability to plan the synthesis strategies, structure design, and composition, which in turn relate to the different applications in materials engineering.

Among the semiconductor oxides, we can mention zinc oxide (ZnO), which is an n-type semiconductor with a direct band gap of 3.37 eV and a large bond cohesion energy of 60 meV at room temperature, thereby being a material with high thermal stability. Furthermore, it is a diamagnetic material, but, when produced at the nanoscale, it exhibits ferromagnetic behavior with high electrical conductivity at room temperature due to a large concentration of defects [4,11]. Ferromagnetism in semiconductor oxides, such as ZnO, remains questionable, since the issues of uniformity and reproducibility have yet to be unraveled, especially because the observed ferromagnetism, which has quite frequently been reported in the literature, can be due to sources other than intrinsic ferromagnetism [12].

The crystal structure of wurtzite-type ZnO is the most thermodynamically stable phase when compared to the zinc blend and rock salt structures. ZnO-wurtzite has a non-centrosymmetric tetrahedral coordination of ZnO and a covalent nature, as well as  $sp_3$  bonding, which are responsible for the semiconductor and piezoelectric behavior [4,11]. Another important feature involves the ferromagnetic coupling mechanism between the spins of TM-3d dopants in the ZnO structure. For example, cobalt (Co) doping can lead to distortion of the ZnO lattice and, when exceeding the Co solubility limit, can lead to cluster formation and the generation of metastable phases such as a ZnO-CoO, where  $Co^{2+}$  ions replace  $Zn^{2+}$  ions. Depending on the synthesis methodology, this can make it possible to obtain phase separation in spinel-type compounds, e.g., ZnO, CoO, and  $Co_3O_4$  [13–17].

The identification and quantification of the physical and chemical properties related to the solubility of TMs in semiconductor oxides necessitate the use of both conventional and unconventional sensitive techniques. Perturbed angular correlation (PAC) spectroscopy is an appropriate powerful hyperfine technique due to its high sensitivity to even small changes in the system, which include local properties such as the electric field gradient (EFG) tensor and magnetic hyperfine field (MHF) contributions. As a result, PAC spectroscopy can obtain data on defects (vacancies and distortions) [18], phase transitions, and diluted clusters in bulk materials [19,20], as well as thin films and nanomaterials [21–23]. PAC, in particular, is a nuclear technique whose signal is unaffected by high temperatures, thereby making it suitable for a variety of environments such as liquid phases, diffusion measurements, and thermodynamic properties. Given the vast body of scientific knowledge on pure ZnO and ZnO doped with TMs, we will list and explain the significance of previous research that was critical to the development of our work.

Mercurio et al. [24] used PAC spectroscopy with  $^{111}Cd$  as a probe to measure hyperfine interactions in ZnO nanoparticles that were systematically doped (where Zn atoms were substituted with cobalt) in concentrations ranging from 5% to 35%, and the resulting  $\nu_Q$  was found to change only slightly as a result of doping. The results were explained in terms of two quadrupole frequencies associated with  $^{111}Cd$  ions occupying two inequivalent crystal sites in the ZnO. The major fraction of  $^{111}Cd$  probes occupied regular positions in the crystal lattice replacing the native Zn atom. At 35% Co doping, the sample exhibited the additional  $Co_3O_4$  phase, because the Co fraction exceeded the solubility limit in the ZnO. The authors compared these results to previous PAC measurements for In-doped ZnO and found that they were very close [25,26].

Photoemission and X-ray absorption spectroscopy studies of ZnO doped with 10% Co [27] confirmed that Co ions replace Zn ions in the regular position of the tetrahedral

symmetric lattice and that both cations remain divalent, thereby demonstrating that there are no significant differences in the electronic structures of pure and Co-doped ZnO. Another study using optical techniques on ZnO nanosheets doped with Co (up to 9%) [28] found that the band gap was analogous to that of pure ZnO (nanosheets and polycrystals forms) and that the crystalline structure remained wurtzite. In the investigation of Co solubility in ZnO thin films using resonant photoemission spectroscopy [29], the authors showed that at a concentration of 15%, a Co cluster with a +3 valence incorporating *d*-states formed in the band gap of the pure ZnO. The introduction of Cd into ZnO was described in a paper reporting characterization using different methods [30]: the decrease in the band gap (up to 10% Cd), the increase in the conductivity and grain size, and the absence of a structural phase transition for concentrations up to 25% Cd.

Muñoz et al. [31] used a theoretical approach to study dynamic interactions (after effects) in pure zinc oxide using first-principles calculations (and complementary PAC measurements). The authors calculated the valence of the Cd ions in the studied oxides for various charge states in supercells and deduced the correspondence between the theoretical and experimental results of the EFG on Cd. In previous papers [32,33], the authors used pseudopotentials to simulate a variety of pure ZnO crystal structure models, thereby employing several parameterizations for the exchange and correlation functional (XC), and they discussed the electronic structure properties under pressure, e.g., the band structure, the density of states (DOS), and the gap energy.

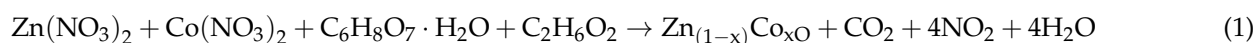
In previous works, the authors simulated two different magnetic arrangements of ZnO doped with Co (ferro- and anti-ferromagnetic coupling) using LDA and LDA + U [34,35], thereby focusing on the magnetic properties. Although the supercells used in these studies [34,35] were smaller than those used this paper, it was demonstrated that a semiconducting behavior in (Co)ZnO exists, in which Co doping does not significantly alter the DOS of pure ZnO. However, Sato et al. [36] reported that the LDA calculations predicted a half-metallic material for several simulated diluted magnetic semiconductors, with ZnO that was doped with some magnetic metals (including Co) exhibiting half-metallic behavior in the DOS.

We present here a comprehensive study that combines PAC spectroscopy, X-ray diffraction, and Ab initio simulations to investigate the role of Co<sup>2+</sup> solid solubility in ZnO. The samples have been prepared using the sol-gel method, which allows us to obtain reproducible results. We carried out X-ray diffractions (XRDs) and PAC measurements using <sup>111</sup>Cd nuclei probes as fingerprints of the local charge density. We also performed Ab initio electronic band structure calculations based on spin-density functional theory (SDFT) formalism.

## 2. Materials and Methods

The samples were synthesized using the well-established Pechini sol-gel method [37]. High-purity metallic elements were employed as starting materials, thereby following the stoichiometric ratio Zn<sub>1-x</sub>Co<sub>x</sub>O (where x = 0, 0.03, 0.05, 0.1, 0.2, 0.25, 0.4, 0.8, and 1 represents the percentage of Co doping). Zinc (Zn) and Cobalt (Co) metals (Alfa Aesar 99.99%) were dissolved in nitric acid (HNO<sub>3</sub>) to form zinc nitrate (Zn(NO<sub>3</sub>)<sub>2</sub>) and cobalt nitrate (Co(NO<sub>3</sub>)<sub>2</sub>) solutions. These solutions were blended with the addition of citric acid (C<sub>6</sub>H<sub>8</sub>O<sub>7</sub>, dissolved in deionized water) and ethylene glycol (C<sub>2</sub>H<sub>6</sub>O<sub>2</sub>), in ratio of 2:1 of product, respectively, according to Equation (1). The resulting solution was heated at 100 °C under magnetic stirring until gel formation, which was subsequently sintered at 400 °C for 10 h in air to obtain a powder sample. After the sintering process, the resulting powder was pressed with 3 tons to form small pellets. These pellets were sealed in quartz tubes under a nitrogen atmosphere (99.99% pure N<sub>2</sub>) and annealed at 600 °C for 12 h. This procedure was followed for each sample.

Equation (1) presents ZnO with Co doping using Pechini sol-gel method:



For PAC measurements, samples were prepared following the same procedure with the difference that approximately 20  $\mu\text{Ci}$  of carrier-free  $^{111}\text{In}$  ( $^{111}\text{Cd}$ ) probe nuclei, in the form of  $^{111}\text{InCl}_3$ , was added to the mixed nitrate solution during synthesis. A small tubular furnace was used for measurements of samples above room temperature, whereas a closed-cycle helium cryogenic device was used to cool it down between 15 and 300 K. After radioactive nuclei decayed, these samples were characterized by XRD using a PANalytical X-ray diffractometer, model X'Pert PRO with X'Celerator detector, using Cu-K $\alpha$  radiation ( $\lambda_{\alpha_1} = 0.154060 \text{ nm}$  e  $\lambda_{\alpha_2} = 0.154443 \text{ nm}$ ) at 40 kV and 40 mA. A step of  $0.05^\circ$  was used for the collection of data.

The well-known  $\gamma - \gamma$  cascade of 171–245 keV, populated from the decay of  $^{111}\text{In}$  to  $^{111}\text{Cd}$  and with an intermediate level at 245 keV ( $T_{1/2} = 84.5 \text{ ns}$  and spin  $I = 5/2^+$ ), was used to investigate the hyperfine interactions using a PAC spectrometer with a conventional fast–slow coincidence setup consisting of four conical BaF $_2$  detectors.

The electric field gradient (EFG) is usually characterized by the major tensor component ( $V_{zz}$ ), which is related to the quadrupole coupling constant  $\nu_Q = eQV_{zz}/h$  and its asymmetry parameter  $\eta = |(V_{xx} - V_{yy})/V_{zz}|$  that varies from 0 to 1 and measures how far from axial symmetry a charge distribution deviates.  $Q$  is the nuclear quadrupole moment, whose latest accepted value is  $Q(^{111}\text{Cd}, 5/2^+) = 0.664(7) \text{ b}$  [38]. Based on the measured time differential gamma–gamma coincidence spectra with detectors at  $90^\circ$  and  $180^\circ$ , it is possible to determine the relevant hyperfine parameters such as EFG, its asymmetry parameter, and MHF, as well as the site fractions ( $f_i$ ) if there are more than one interaction. Further details about the description of the PAC method, as well the treatment of data, can be found from Refs. [39–41].

The simulation of a wide range of scenarios of Co solid solubility in ZnO required the use of a periodic supercell (SC) approach, where a series of large structures with periodic conditions were generated from the  $3 \times 3 \times 2$  replication of the conventional ZnO unit cell (UC) along the Cartesian axes. Figure 1 shows an example based on an illustration created in the XCRYSDEN software [42]. Considering the system's magnetic moment, we included the spin polarization in the calculations. The computational implementation was performed using the full potential linearized augmented plane wave plus local orbital (APW+ $lo$ ) scheme [43] within the WIEN2k code [44], where the exchange correlation (XC) potentials were described through the local-density approximation (LDA) and generalized gradient approximation (GGA) of Perdew–Burke–Ernzerhoff (PBE) [45] and Wu–Cohen (WC) [46]; details of the theoretical procedure are now summarized.

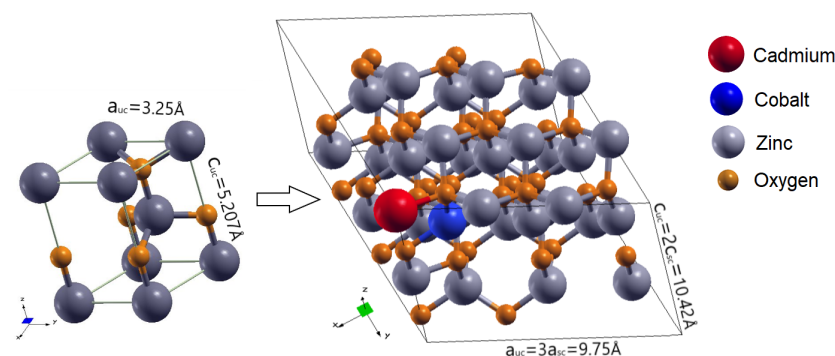


**Figure 1.** A schematic representation of the standard crystal structures employed for Ab initio calculations. (Left): ZnO unit cell (UC). (Right):  $3 \times 3 \times 2$  ZnO supercell (SC).

The atomic spheres radii ( $R_{\text{MT}}$ ) used here (in bohr) were  $R_{\text{MT}}^{\text{Zn}} = 1.88$ ,  $R_{\text{MT}}^{\text{Cd}} = 2.03$ ,  $R_{\text{MT}}^{\text{Co}} = 1.85$ , and  $R_{\text{MT}}^{\text{O}} = 1.64$ . For better convergence, the cutoff parameter  $R_{\text{MT}}^{\text{O}} K_{\text{MAX}}$  was set to 7, and a  $k$ -points sampling of up to 150 points in the Brillouin zone (BZ) was used. The optimized lattice parameters predicted by APW+ $lo$  revealed values practically identical to the experimental ones [47]. Finally, in order to obtain representative models that describe the hyperfine parameters, a possible deep impurity acceptor or donor level

in the band gap when host elements are replaced by dopants must be considered. As a result, we made calculations for various charge states of the SCs. Furthermore, because the supercell contains different types of covalent and ionic radii, an expressive lattice distortion in internal parameters is expected. To obtain the equilibrium atomic positions where the Hellmann–Feynman forces on atoms would be less than  $0.01 \text{ eV}/\text{\AA}$ , an extensive energy minimization process was carried out. The EFG tensor's main components were calculated directly from the multipole expansion of the Coulomb potential, as described by Blaha et al. [48].

### 3. Results and Discussion

#### 3.1. Experimental Results: XRD and PAC Measurements in Undoped and Co-Doped ZnO

In order to check the quality of the synthesized Co doped in ZnO samples, PAC spectra at room temperature were recorded. The analysis of the  $R(t)$  spectra for pure ZnO (Figure 2a) and ZnO samples doped (alloyed) with up to 25% Co (Figure 2b) were fitted considering only quadrupole interactions for all the site fractions ( $f_i$ ). The well-defined quadrupole frequency in the  $R(t)$  spectra,  $\nu_Q \simeq 33 \text{ MHz}$  ( $V_{zz} = 1.99 \times 10^{21} \text{ Vm}^{-2}$ ), is a fingerprint of  $^{111}\text{Cd}^{2+}$  probe nuclei in an environment which can be attributed to the regular substitutional  $\text{Zn}^{2+}$  sites in the crystalline lattice of ZnO belonging to the space group  $P63mc$  [24,25].

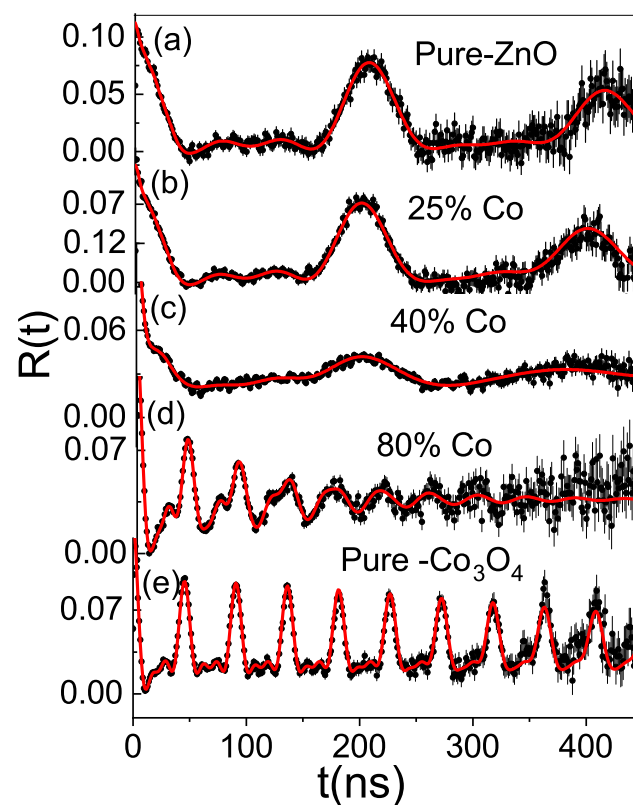


**Figure 2.** PAC spectra collected from sample B at room temperature for  $^{111}\text{In}$ - $^{111}\text{Cd}$  probe nuclei in pure and Co-doped ZnO as indicated by concentration (atoms %). The solid lines are the least square fits to the theoretical function.

For the  $R(t)$  spectra observed above 25% Co-doped ZnO samples, a damped behavior was observed. The analysis of these spectra revealed a decrease in the fraction of the probe nuclei at the  $^{111}\text{Cd}^{2+}$  in ZnO, as well as the need for two additional sites to provide a good fit to the experimental data (see Figure 2c). Consequently, the fit results show a *site-1* with a population of  $f_1 = 37\%$ , which was characterized by a quadrupole frequency of  $\nu_{Q1} \simeq 32 \text{ MHz}$  and asymmetry,  $\eta = 0.28$ ; this was most likely due to a distorted environment

caused by the high doping concentration. The additional *site-2* corresponded to  $^{111}\text{Cd}^{2+}$  in a cubic crystalline environment with  $\nu_{Q2} \simeq 5$  MHz and  $f_2 = 6\%$ . This site fraction was ascribed to  $^{111}\text{Cd}^{2+}$  replacing  $\text{Co}^{2+}$  in *fcc*-CoO rock salt, because magnetic interactions are absent in *fcc*-CoO at room temperature, and the cubic environment yields a zero EFG [23]. The *site-3* showed a  $\nu_{Q3} \simeq 152$  MHz with  $f_3 = 57\%$  but a very high frequency distribution of  $\delta = 50\%$ , thereby indicating a low degree of crystallinity or a high degree of disorder.

In addition, in order to develop a better understanding of the Co dilution data in ZnO and to identify additional phases, two  $\text{Co}_3\text{O}_4$ -rich samples were synthesized following the same Co-doped ZnO synthesis procedure. The  $R(t)$  spectra for the cobalt-rich regions presented a single and well-defined quadrupole frequency of  $\nu_{Q1} = 147$  MHz with  $\delta_1 = 1\%$  ( $V_{zz} = 9.17 \times 10^{21} \text{ Vm}^{-2}$ ) and a very low asymmetry parameter  $\eta_1 = 0.05$  (see Figure 2d,e). These hyperfine parameters are characteristic of  $^{111}\text{Cd}^{2+}$  replacing the ( $\text{Co}^{2+}$ ) substitutionally at the octahedral site in the spinel lattice of  $\text{Co}_3\text{O}_4$  [49]. However, at 80% Co (Figure 2d), a good fit of the spectrum was obtained using, in addition to the  $^{111}\text{Cd}^{2+}$  at the octahedral site ( $f = 54\%$ ), a second site fraction with a high frequency distribution ( $\delta = 40\%$ ) and population of  $f = 46\%$ . This site with a wide frequency distribution is usually related to a noncrystalline environment or could be related to probe nuclei that did not diffuse properly throughout the samples, thereby residing instead in sites near the grain boundary and/or intrinsic defects in the sample.

X-ray diffraction (XRD) patterns recorded after the decay of the radioactive probe nuclei also confirmed the presence of additional phases. These patterns confirmed the presence of cobalt oxide in the dilution limit region of the Co in ZnO (see Figure 3) for both cobalt concentrations of 25% and 40%, where a small fraction of  $\text{Co}_3\text{O}_4$  and a high fraction of *fcc*-CoO were present in the samples.

In the threshold Co solubility, according to Figure 4, the line with a positive slope indicates an increase in the degree of distortion (R) in wurtzite-structure ZnO with increasing Co concentration. This result is similar to the previous report by Kumar et al. [50]. A slow linear variation in the degree of distortion can be attributed to the small difference in the ionic radii between the substitution of the  $\text{Zn}^{2+}$  (0.60 Å) by  $\text{Co}^{2+}$  (0.58 Å) [51], which results in a contraction in the cell parameter (c) and a slight elongation in (a). The line with a negative slope represents a decrease in the c/a ratio variation of the cation–anion bond length to Co ions, thereby showing that the c/a ratio of the hexagonal structure decreases with the corresponding increase of Co concentration. This results in the development of a tolerable tensile stress in the sample, thereby leading to an improvement of the ionic character in X–O bonding (X = Zn, Co) with Co doping.

Note that in the Co solubility limits, the XRD results confirm a single-phase with a space group  $P63mc$ . Similar results were observed by Mesquita et al. [52], where the appearance of a CoO phase was detected for Co concentrations higher than 25%. The PAC and XRD results support the presence of a CoO–rock salt phase. However, we did not obtain specific information about the spinel– $\text{Co}_3\text{O}_4$  phase. Nevertheless, it is essential not to identify phases observed in XRD, using the fractions ( $f_1, f_2, f_3$ ) observed by PAC spectroscopy, because the fractions of  $^{111}\text{Cd}$  are dependent on the chemical and physical affinity of the probe nuclei with the crystalline environment. As a result, we can have a phase that is barely observed in XRD but with a high fraction of probe nuclei or vice versa.

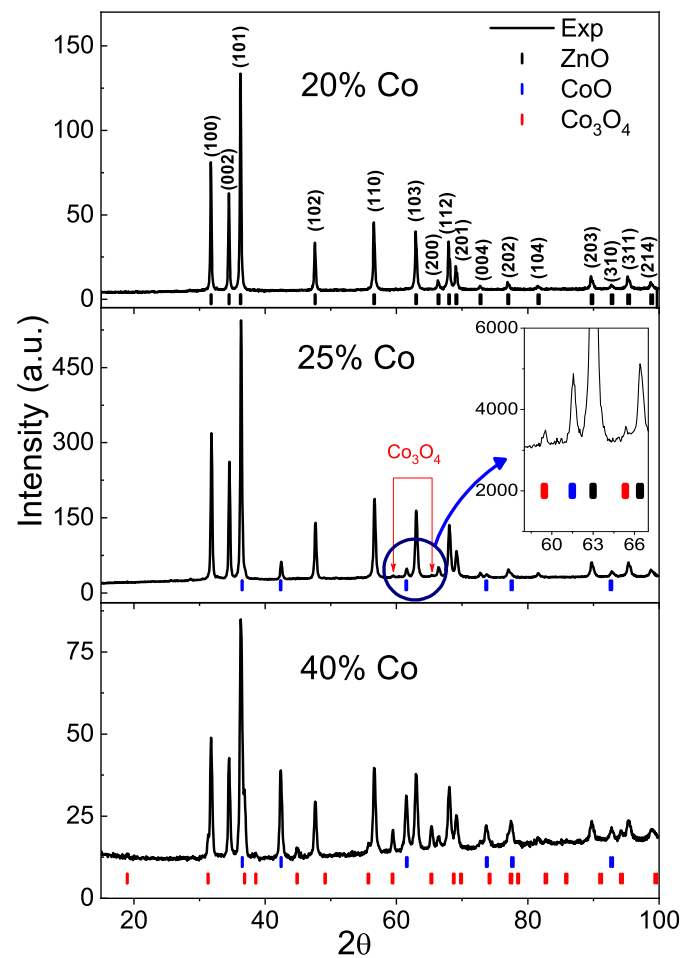


**Figure 3.** X-ray diffraction patterns of Co-doped ZnO as indicated by concentration (atoms %) obtained in sample B. The marks represent the position of the Bragg interference peaks. The inset is to enhance the  $\text{Co}_3\text{O}_4$  phase for the 25% Co concentration.

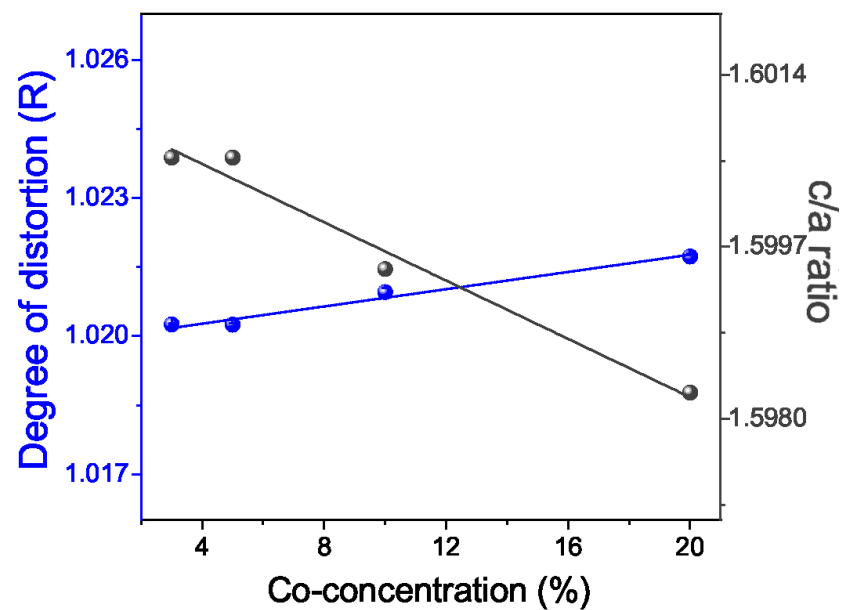


**Figure 4.** Variation in the degree of distortion (R) (in blue) and ratio between lattice parameter (c/a) (in gray).

In Figure 5, we show the hyperfine parameters of the samples obtained from the PAC spectra for various Co concentrations. The small values of  $\eta$  and  $\delta$  (frequency distribution parameters) and  $\lambda$  (parameter indicating the presence of dynamic interactions) in these data indicate that the probe nuclei at the substitutional Zn sites have high axial symmetry, a narrow frequency distribution, and a small dynamic interaction. However, as shown in Figure 5a,b, as the cobalt concentrations increased,  $\nu_Q$  and  $\eta$  increased, thereby indicating a possible shift from the hexagonal structure of the ZnO lattice in the near-neighbor environment of the  $^{111}\text{Cd}$  atoms. The quadrupole frequency ( $\nu_Q$ ) changed very little from pure to 3% Co-doped samples, with both falling below 32 MHz, as shown in Figure 5a. This finding suggests that, although the asymmetry ( $\eta_{\text{pure}} \lesssim \eta_{\text{doped}}$ ) changed slightly, the probe nuclei  $^{111}\text{Cd}$  did not interact with the dopant, and, thus, doped ZnO below 3% behaved like a pure sample. A small increase in  $\nu_Q$  was observed for 3% to 20% Co, where it reached an almost saturation frequency around 33 MHz. This increase, along with the increase in  $\eta$ , is attributed to the presence of Co dopants in the vicinity of the probe nuclei, and it saturates for Co concentrations greater than 20% due to the formation of cobalt oxide clusters, as observed by XRD (see Figure 3 and Ref. [52]).

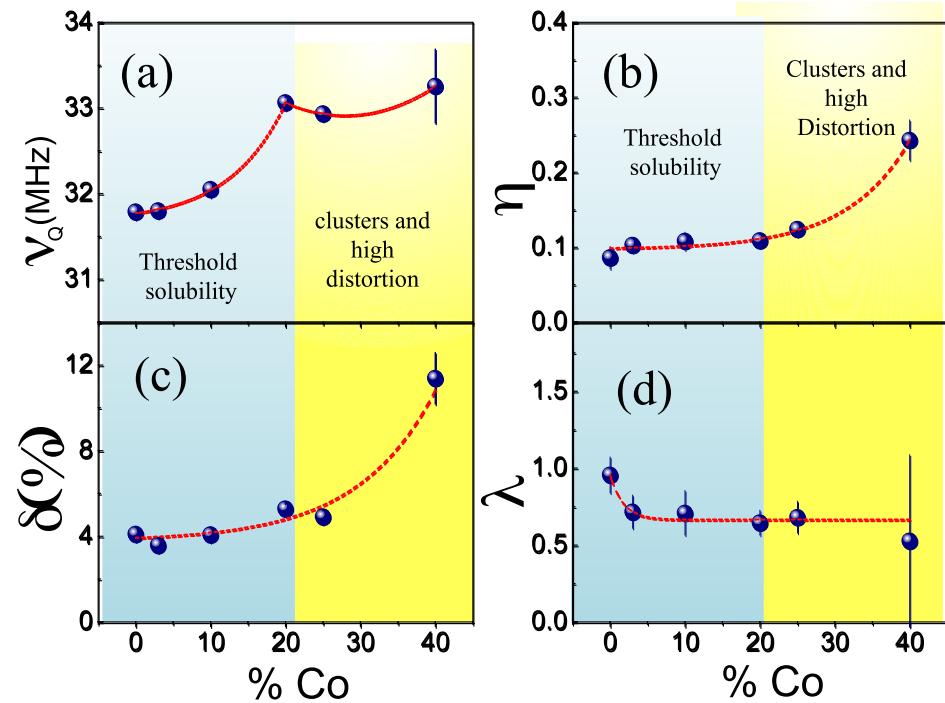


**Figure 5.** Dependence on the cobalt concentration of the hyperfine parameters obtained using PAC data collected at room temperature for samples: (a) quadrupole frequency  $\nu_Q$  (MHz); (b) asymmetry parameter  $\eta$ ; (c) frequency distribution parameter  $\delta$  (%); and (d) dynamic interaction  $\lambda$  (MHz).

### 3.2. Ab Initio Results: EFG Predictions and DOS Calculations

According to the methodology proposed for the Co solubility effects in ZnO within the SDFT scheme, we present a systematic analysis of the EFGs of Zn-Cd substitutional sites, as well as the electronic density of states (DOS) composition of the supercells. Table 1 shows the EFG predictions of the ZnO-Cd and ZnO-Cd-Co supercells.



**Table 1.** Predicted EFG component  $V_{zz}$  (in  $10^{21}$   $\text{Vm}^{-2}$ ) at Cd probe in supercells of ZnO, thereby considering three- and one-charge states for representations of undoped and Co-doped ZnO samples, respectively. The EFG experimental results reported in this work and Ref. [24] are included for comparison purposes.

EFG	XC-LDA	XC-PBE	XC-WC
		[ZnO-Cd] <sup>1-</sup>	
$V_{zz}$	1.31		
$\eta$	0		
		[ZnO-Cd] <sup>1+</sup>	
$V_{zz}$	1.07		
$\eta$	0		
		[ZnO-Cd] <sup>0</sup>	
$V_{zz}$	1.43	1.15	1.68
$\eta$	0	0.14	0
		[ZnO-Cd-Co] <sup>0</sup>	
$V_{zz}$	1.55	1.12	1.81
$\eta$	0.62	0.15	0.29
EFG exp. data:	Pure ZnO	$V_{zz} \simeq 1.99$	$\eta \simeq 0$
	Pure ZnO [24]	$V_{zz} \simeq 1.93$	$\eta \simeq 0$
	20% Co in ZnO	$V_{zz} \simeq 1.99$	$\eta \simeq 0$
	40% Co in ZnO	$V_{zz} \simeq 1.25$	$\eta \simeq 0.28$

We started considering a first scenario without the Co doping, i.e., one Zn atom was replaced by one Cd “probe” atom in the supercell. For this, we simulated supercells assuming a “neutral charge state” by adding and removing electrons. The APW+*lo* predictions show that in the neutral supercells for the three XC functionals the EFG’s computation were very similar to each other and to the experimental EFG results of this paper (Figure 1a,b) and those of Mercurio et al. [24]. It is interesting to note that there was no systematic relation between the impurity valence and the  $V_{zz}$ , because when we compared the  $V_{zz}$  in the neutral supercell with respect to the charged supercells, a less accurate prediction of the  $V_{zz}$  values was obtained; thus, the  $V_{zz}$  in the neutral supercell had the best agreement with experimental measurements. It can be inferred that in the experiments the real charge state of the Cd in the ZnO samples is 2+. Also, this was demonstrated in a dynamic hyperfine interactions study [31] where the Cd impurity decayed to the final neutral charge state ( $\text{Cd}^{2+}$ ) in pure ZnO.

We then considered the second scenario where the Co solubility effects were included, wherein we replaced one Zn atom of the structure with Co; for a neutral charge state, there was no significant change in the EFG tensors between the ZnO-Cd and ZnO-Cd-Co supercells (see Table 1): The  $V_{zz}$  computation varied subtly, while the symmetry the EFG tensors ( $\eta$ ) was practically the same for all functionals except the LDA. As can be seen in angular correlation patterns in the PAC spectra, a low asymmetry parameter ( $\eta \sim 0.1$ ) was observed, and our predictions corroborate that this is associated with the Co impurities that induce a small local geometrical distortion in the host lattice.

In general, the EFG calculations for ZnO-Cd-Co supercell agree with previous experimental results of PAC [24] and photoemission spectroscopy [27] for a wide range of Co doping in ZnO, where  $V_{zz}$  has been shown to be practically unchanged. Indeed, we built the ZnO supercell using two dopants (second-shell atoms) as the first cationic neighbors. Cadmium and cobalt additions in the supercell resulted in a broken symmetry leading to only one symmetry operation. Then, from a symmetry perspective, replacing any Zn atoms with Co is equal, meaning that the doping at the second neighborhood of cadmium can be accomplished with (i) one Co atom in a different position of the Zn or (ii) two or more Co atoms at Zn sites. This is because all zinc atoms that are second neighbors of cadmium have the same point group. Furthermore, the result would remain the same even if (iii) at the Cd fourth neighborhood, there were one or more Co atoms; the supercell’s space group would not change. As is well known, the hyperfine interaction parameters are

very sensitive to the local surroundings and the EFG tensors decrease with the cube of the distance of the charges from the nucleus. Thus, taking these two concepts into account, we did not simulate the (ii) and (iii) scenarios because our experimental systems had several Co concentrations, and the Cd EFG values for those samples were, in general, independent of the Co doping up to 20%—above which the  $\text{Co}_x\text{O}_y$  and ZnO separation occurs.

After the explanations about the EFG in this work, we gave more confidence to this Ab initio study through the analysis of the DOS compositions (Figures 6 and 7) for understanding how the impurity levels of Cd and Co ions affect the band structure of the ZnO as follows.

Upon analyzing the results, it is possible to observe that the introduction of Cd in pure ZnO (Figure 6) generates a sharp peak that is spatially confined between the energies of  $-6$  to  $-7$  eV, where the valence band (according to the (a) and (b) insets in the Figure 6), moves directly above the Fermi level, thereby decreasing the gap from 2.2 eV to 1.0 eV and following a general trend of narrowing the band gap already reported in experimental and Ab initio studies of Cd doped in ZnO [30,53,54]. This theoretical approach was also validated by comparing our predictions with GGA+U calculations [55], in which the authors introduced the U potential to improve the gap prediction in ZnO supercells with Cd doping concentrations ranging from 2–25% and in a similar way as observed in this paper; the impurity level did not significantly change the band structure of the system, thereby showing DOS curves of the same shape and thus preserving the semiconductor character.

Proceeding with the analysis, we present the DOS graphs obtained from the ZnO-Cd-Co supercell (Figure 7); a half-metallic behavior can be noted that suppressed the gap that was once observed in the DOS composition (Figure 6) for the ZnO and ZnO-Cd calculations. In the meantime, previous works in photoemission spectroscopy [27] and LDA+U calculations [34] demonstrated that ZnO impurified by cobalt remained a semiconductor just like pure ZnO (for a more detailed discussion, (see Supplementary Materials). In the inset (a) of Figure 7, we can see that the DOS contributions of Cd (red line) and Co (green line) are small in the energy range, which corresponds to the band characteristic of the pure ZnO. By means of this inset image, it becomes clear that around the Fermi level the valence band (VB) top and conduction band (CB) bottom are dominated by the impurity levels of Cd and Co ions (which are partially filled) coexisting on the same energy range. There is also another interaction band between Cd and Co; it is defined at  $-8.5$  eV, which is exactly at the main impurity level of the Cd in DOS. Since these impurity levels are completely hybridized with the levels corresponding to the ZnO crystal matrix, the Cd ion “sees” its Co dopant neighbor, whose most important interaction between them occurs in the characteristic band of ZnO (responsible for the origin of the EFG), where the threshold solubility corroborated by the fully hybridized state compositions in the DOS provide clear proof that the systematic addition of Co slightly alters the electric field gradient of ZnO and the local environment around the Cd probe, thereby justifying the slight variation in the EFG reported in this paper.

The Refs. [35,36] show the DOS composition for supercells with larger Co doping concentrations (above the threshold solubility), where the research focus was aimed mainly to clarify the Co-Co interactions; however (just like this work), the authors found that their calculations with LDA presented errors, thereby establishing half-metallic behavior in ZnO-Co. This is in contrast to what we visualize in the inset (b) of the Figure 7, which indicates metallic behavior with the same number of electrons for the spins up/down, both at the Fermi level and in the other bands, thereby implying a magnetic moment equal to zero for our ZnO-Co supercell. In the meantime, after comparing both our results and those mentioned, it appears that they do not match the experiment.

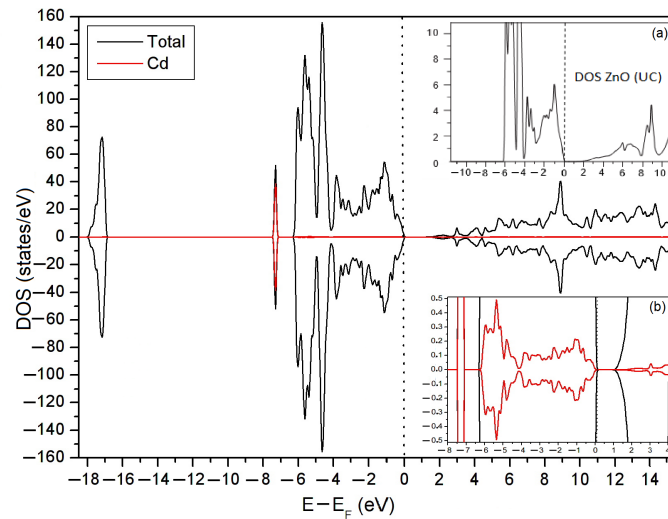


**Figure 6.** Calculated total DOS and projected DOS of the Cd ion for ZnO-Cd SC predicted by the GGA-PBE functional. Inset (a): The calculated total DOS of the ZnO UC employed in this work is included for comparison purposes. Inset (b): The highlighted graph makes it easy to see the curves in the range  $-8$  to  $4$  eV. The Fermi level is indicated by the vertical dot line at  $0$  eV.

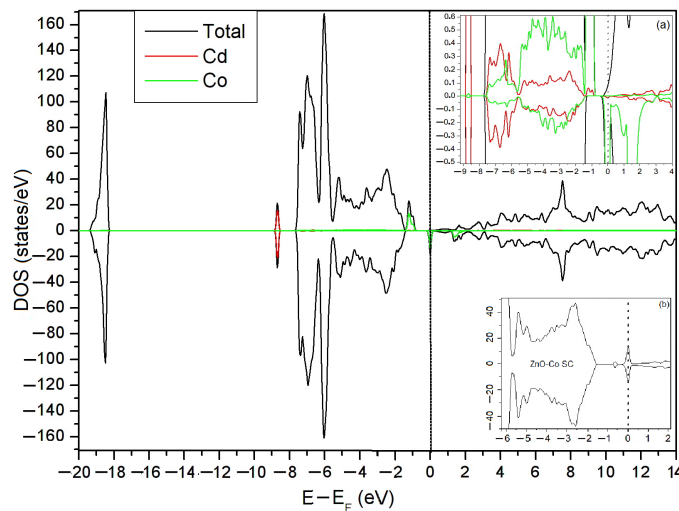


**Figure 7.** Calculated total DOS and projected DOS of the Cd and Co ions for ZnO-Cd-Co SC predicted by the GGA-PBE functional. Inset (a): The highlighted graph makes it easy to see the curves in the range  $-9$  to  $4$  eV. Inset (b): The calculated total DOS of the ZnO-Co SC employed in this work is included for comparison purposes. The Fermi level is indicated by the vertical dot line at  $0$  eV.

Here is a caveat regarding the false half-metallic ferromagnetic state of the Co: this well-known error in band theory prediction is intrinsic to the XC potentials, and our accurate predictions with respect to the experimental results validate the use of these standard functionals applied in our simulations, even if in the absence of strongly correlated methods in XC functionals. When directly treating the electronic correlation in a given cation site (DFT + U), it is possible to determine the magnetic moment in nonmagnetic TMO's impurified by magnetic probes. For example, by employing LDA + U calculations in ZnO-Co [34], it was possible to obtain the magnetic moment of  $\mu_{Co} = 2.8 \mu_B$ ; this value is reasonable to the experimental  $\mu_{Co}$  in CoO [56]. It is noteworthy, as shown in Figure 7, that the DOS curves around the Fermi level for the Co states spins up/down were not identical, thereby indicating that the ZnO-Cd-Co supercell exhibited a magnetic moment; the value found was  $3.02 \mu_B$ , thus agreeing very well with Refs. [34,56].

According to the inset image (a) of Figure 7, the small spin decomposition in the Cd states that comes from hybridization with  $O_{Cd-Co}$  present at the top of the VB was not enough to generate an expressive magnetic moment, which was very close to zero ( $0.0017 \mu_B$ ); this explains why we did not predict the HFF transferred from the Cd. In this context, there is still debate concerning the origin of the ferromagnetic response in DMS [57–61], whereas Zn and Cd had many similar chemical properties. Our results for the TM-doped ZnO indicate that about certain circumstances related to the nonextreme environments acting in the experiment; it can be concluded that the enhanced magnetic response in ZnO through Co doping still remains unclear. Further studies also are needed to establish a control mechanism in carrier-mediated versus defect-mediated transport and thus distinguish between extrinsic and intrinsic defects induced as being due, respectively, to the direct interaction between the local moments in magnetic impurities and the exchange coupling between spin carriers and local magnetic moments.

#### 4. Conclusions

Through Ab initio calculations and PAC spectroscopy, we have showed that the EFG is a great monitoring tool for mapping of the threshold Co solubility in ZnO. In our PAC measurements, Co-doped ZnO samples showed a single phase ZnO structure with up to 20% Co concentration, as corroborated by XRD. Above this concentration, X-ray results confirmed the occurrence of the segregation of ZnO/CoO/Co<sub>3</sub>O<sub>4</sub> phases, while PAC showed strong distortions and a damping in the spectra. For ZnO with 40% Co, we obtained through the PAC technique weak evidence of Co<sub>3</sub>O<sub>4</sub> due to the low fraction of this phase.

By means of SDFT calculations using APW+*lo* methodology, it was possible to obtain a prediction of the electronic structure of ZnO focusing on the EFG computation and DOS composition. The systematic supercell modeling was made according to the need of representation of the PAC experiments; therefore, the study of ZnO doped by Co and/or Cd was done by modeling ZnO crystals with a single dopant and double doping (Cd and Co being neighbors). Thus, using three XC functionals, we observed that the EFG values in the two systems with Cd (ZnO-Cd and ZnO-Cd-Co) were equivalent to the experimental results on the undoped and Co-doped ZnO samples. The presence of Cd radically did not change the DOS of pure ZnO, and, thus, the ZnO-Cd system remains as semiconducting. Nevertheless, when one Co is added (ZnO-Co and ZnO-Cd-Co), there is a modification in the electron energy levels that yields a half-metallic behavior, but due to the complete hybridization of the Co states with the characteristic band of the ZnO, this does not generate expressive changes in the EFG tensor ( $V_{zz}$ ), thereby predicting within the threshold Co solubility an axially symmetric Cd site ( $\eta = 0$ ) and asymmetrical Cd site ( $\eta \neq 0$ ) and containing distortions as a consequence of Co doping above the solubility threshold, thus corroborating experimental results.

**Supplementary Materials:** The following supporting information can be downloaded at <https://www.mdpi.com/article/10.3390/cryst14010051/s1>, Figure S1: Calculated projected DOS on some ions for ZnO-Cd-Co SC. Figure S2: Calculated total DOS and projected DOS of the Cd and Co ions for ZnO UC. Figure S3: Calculated projected DOS of the Zn-3d states and O-2p states for ZnO UC. References [18,62–64] are cited in the Supplementary Materials.

**Author Contributions:** Conceptualization, L.F.D.P., W.L.F., G.A.C.-P. and A.W.C.; methodology, L.F.D.P., M.S.C. and A.W.C.; validation, M.S.C., W.L.F., A.B., B.B.-S. and C.S.C.; formal analysis, W.L.F., L.F.D.P., G.A.C.-P., A.B. and A.W.C.; investigation, L.F.D.P., T.S.N.S., A.A.M.F., M.S.C., B.B.-S. and C.S.C.; data curation, L.F.D.P., W.L.F., B.S.C. and G.A.C.-P.; writing—original draft preparation, W.L.F., M.S.C. and L.F.D.P.; writing—review and editing, W.L.F., B.S.C., G.A.C.-P., J.S. and A.W.C.; visualization, G.A.C.-P., W.L.F., B.S.C., L.F.D.P. and M.S.C.; supervision, G.A.C.-P., J.S., R.N.S. and A.W.C.; project administration, R.N.S. and A.W.C.; funding acquisition, R.N.S. and A.W.C. All authors have read and agreed to the published version of the manuscript.

**Funding:** This research was funded by the Fundação de Amparo a Pesquisa do Estado de São Paulo (FAPESP) through grants numbers 2012/11104-9, 2014/14001-1, and 2017/50332-0, and W.L.F. acknowledges the Coordenação de Aperfeiçoamento de Pessoal de Nível Superior (CAPES) for financial support in the form of a scholarship through grant number 88887513796/2020-00. B.S.C. and A.W.C. acknowledge the Conselho Nacional de Desenvolvimento Científico e Tecnológico (CNPq) for financial support through grant numbers 142070/2019-0 and 307322/2021-1, respectively. L.F.D.P. expresses his thanks to CNPq for financial support in the form of a Fellowship (Grant No. 444323/2018-0 of the Programa de Capacitação Institucional-PCI). J.S. and B.S.C. acknowledge the financial support received from the Federal Ministry of Education and Research (BMBF) through grants No. 05K16PGA and 05K22PGA, respectively.

**Data Availability Statement:** Data are available upon request.

**Conflicts of Interest:** The authors declare no conflicts of interest.

## References

1. Lee, J.-H.; Ko, K.-H.; Park, B.-O. Electrical and optical properties of ZnO transparent conducting films by the sol–gel method. *J. Cryst. Growth* **2003**, *247*, 119–125. [[CrossRef](#)]
2. Matsubara, K.; Fons, P.; Iwata, K.; Yamada, A.; Sakurai, K.; Tampo, H.; Niki, S. ZnO transparent conducting films deposited by pulsed laser deposition for solar cell applications. *Thin Solid Film*. **2003**, *431*, 369–372. [[CrossRef](#)]
3. Ryu, H.-W.; Park, B.-S.; Akbar, A.S.; Lee, W.-S.; Hong, K.-J.; Seo, Y.-J.; Shin, D.-C.; Park, J.-S.; Choi, G.-P. ZnO sol–gel derived porous film for CO gas sensing. *Sens. Actuators B Chem.* **2003**, *96*, 717–722. [[CrossRef](#)]
4. Verma, K.C. Diluted Magnetic Semiconductor ZnO: Magnetic Ordering with Transition Metal and Rare Earth Ions. In *Magnetic Materials and Magnetic Levitation*; IntechOpen: Rijeka, Croatia, 2021; p. 109.
5. Akshay, V.R.; Arun, B.; Mandal, G.; Vasundhara, M. Structural, optical and magnetic behavior of sol–gel derived Ni-doped dilute magnetic semiconductor TiO<sub>2</sub> nanocrystals for advanced functional applications. *Phys. Chem. Chem. Phys.* **2019**, *21*, 2519–2532. [[CrossRef](#)] [[PubMed](#)]
6. Hou, D.; Meng, H.J.; Jia, L.Y.; Ye, X.J.; Zhou, H.J.; Li, X.L. Oxygen vacancy enhanced the room temperature ferromagnetism in Ni-doped TiO<sub>2</sub> thin films. *Phys. Lett. A* **2007**, *364*, 318–322. [[CrossRef](#)]
7. Sonomura, H.; Uragaki, T.; Miyauchi, T. Synthesis and Some Properties of Solid Solutions in the GaP–ZnS and Gap–ZnSe Pseudobinary Systems. *Jpn. J. Appl. Phys.* **1973**, *12*, 968. [[CrossRef](#)]
8. Jagodič, M.; Jagličić, Z.; Jelen, A.; Lee, J.B.; Kim, Y.-M.; Kim, H.J.; Dolinšek, J. Surface-spin magnetism of antiferromagnetic NiO in nanoparticle and bulk morphology. *J. Phys. Condens. Matter*. **2009**, *21*, 215302. [[CrossRef](#)]
9. Morales, M.A.; Skomski, R.; Fritz, S.; Shelburne, G.; Shield, J.E.; Yin, M.; O’Brien, S.; Leslie-Pelecky, D.L. Surface anisotropy and magnetic freezing of MnO nanoparticles. *Phys. Rev. B* **2007**, *75*, 134423. [[CrossRef](#)]
10. Gupta, A.; Zhang, R.; Kumar, P.; Kumar, V.; Kumar, A. Nano-structured dilute magnetic semiconductors for efficient spintronics at room temperature. *Magnetochemistry* **2020**, *6*, 15. [[CrossRef](#)]
11. Janotti, A.; Van de Walle, C.G. Fundamentals of zinc oxide as a semiconductor. *Rep. Prog. Phys.* **2009**, *72*, 126501. [[CrossRef](#)]
12. Pereira, L.M.C.; Araújo, J.P.; Van Bael, M.J.; Temst, K.; Vantomme, A. Practical limits for detection of ferromagnetism using highly sensitive magnetometry techniques. *J. Phys. D Appl. Phys. D* **2011**, *44*, 215001. [[CrossRef](#)]
13. Kundaliya, D.C.; Ogale, S.B.; Lofland, S.E.; Dhar, S.; Metting, C.J.; Shinde, S.R.; Ma, Z.; Varughese, B.; Ramanujachary, K.V.; Salamanca-Riba, L.; et al. On the origin of high-temperature ferromagnetism in the low-temperature-processed Mn–Zn–O system. *Nat. Mater.* **2004**, *3*, 709–714. [[CrossRef](#)] [[PubMed](#)]
14. Coey, J.M.D.; Venkatesan, M.; Fitzgerald, C.B. Donor impurity band exchange in dilute ferromagnetic oxides. *Nat. Mater.* **2005**, *4*, 173–179. [[CrossRef](#)] [[PubMed](#)]
15. Djerdj, I.; Jagličić, Z.; Arčon, D.; Niederberger, M. Co-doped ZnO nanoparticles: Minireview. *Nanoscale* **2010**, *2*, 1096–1104. [[CrossRef](#)] [[PubMed](#)]
16. Wojnarowicz, J.; Kusnieruk, S.; Chudoba, T.; Gierlotka, S.; Lojkowski, W.; Knoff, W.; Lukaszewicz, M.I.; Witkowski, B.S.; Wolska, A.; Klepka, M.T.; et al. Paramagnetism of cobalt-doped ZnO nanoparticles obtained by microwave solvothermal synthesis. *Beilstein J. Nanotechnol.* **2015**, *6*, 1957–1969. [[CrossRef](#)] [[PubMed](#)]
17. Nayak, S.; Kumar, P. Review on structure, optical and magnetic properties of cobalt doped ZnO nanoparticles. *Mater. Today Proc.* **2023**, *in press*. [[CrossRef](#)]
18. Ferreira, W.L.; Pereira, L.F.D.; Neto, O.F.S.L.; Maciel, L.S.; Gonçalves, V.C.; Saxena, R.N.; Carbonari, A.W.; Costa, M.S.; Cabrera-Pasca, G.A. Locally symmetric oxygen vacancy around Cd impurities in CeO<sub>2</sub>. *Phys. Rev. B* **2021**, *104*, 035–146. [[CrossRef](#)]
19. Schell, J.; Schmuck, M.; Efe, I.; Dang, T.T.; Gonçalves, J.N.; Lewin, D.; Castillo, M.E.; Shvartsman, V.V.; Costa, A.R.G.; Köster, U.; et al. Strong magnetoelectric coupling at an atomic nonmagnetic electromagnetic probe in bismuth ferrite. *Phys. Rev. B* **2022**, *105*, 94–102.
20. Sena, C.; Costa, M.S.; Muñoz, E.L.; Cabrera-Pasca, G.A.; Pereira, L.F.D.; Mestnik-Filho, J.; Carbonari, A.W.; Coaquira, J.A.H. Charge distribution and hyperfine interactions in the vicinity of impurity sites in In<sub>2</sub>O<sub>3</sub> doped with Fe, Co, and Ni. *J. Magn. Mater.* **2015**, *387*, 165–178. [[CrossRef](#)]

21. Corrêa, B.S.; Costa, M.S.; Cabrera-Pasca, G.A.; Sena, C.; Holanda Pinto, R.H.; Silva, A.P.S.; Carvalho Junior, R.N.; Ishida, L.; Ramon, J.G.; Freitas, R.S.; et al. High-saturation magnetization in small nanoparticles of Fe<sub>3</sub>O<sub>4</sub> coated with natural oils. *J. Nanoparticle Res.* **2020**, *22*, 68. [[CrossRef](#)]
22. Campos, A.C.; Paes, S.C.; Correa, B.S.; Cabrera-Pasca, G.A.; Costa, M.S.; Costa, C.S.; Otubo, L.; Carbonari, A.W. Growth of long ZnO nanowires with high density on the ZnO surface for gas sensors. *ACS Appl. Nano Mater.* **2019**, *3*, 175–185. [[CrossRef](#)]
23. Santos, R.V.; Cabrera-Pasca, G.A.; Costa, C.S.; Bosch-Santos, B.; Otubo, L.; Pereira, L.F.D.; Correa, B.S.; Effenberger, F.B.; Burimova, A.; Freitas, R.S.; et al. Crystalline and magnetic properties of CoO nanoparticles locally investigated by using radioactive indium tracer. *Sci. Rep.* **2021**, *11*, 21028. [[CrossRef](#)] [[PubMed](#)]
24. Mercurio, M.E.; Carbonari, A.W.; Cordeiro, M.R.; Saxena, R.N.; D'Agostino, L.Z. Local investigation of hyperfine interactions in pure and Co-doped ZnO. *J. Magn. Magn. Mater.* **2010**, *322*, 1195–1197. [[CrossRef](#)]
25. Agne, T.; Guan, Z.; Li, X.M.; Wolf, H.; Wichert, T.; Natter, H.; Hempelmann, R. Doping of the nanocrystalline semiconductor zinc oxide with the donor indium. *Appl. Phys. Lett.* **2003**, *83*, 1204–1206. [[CrossRef](#)]
26. Sato, W.; Takata, M.; Shimizu, H.; Komatsuda, S.; Yoshida, Y.; Moriyama, A.; Shimamura, K.; Ohkubo, Y. Atomic level control of association-dissociation behavior of In impurities in polycrystalline ZnO. *Phys. Rev. Mater.* **2022**, *6*, 063801. [[CrossRef](#)]
27. Wi, S.C.; Kang, J.-S.; Kim, J.H.; Cho, S.-B.; Kim, B.J.; Yoon, S.; Suh, B.J.; Han, S.W.; Kim, K.H.; Kim, K.J.; et al. Electronic structure of Zn<sub>1-x</sub>Co<sub>x</sub>O using photoemission and X-ray absorption spectroscopy. *Appl. Phys. Lett.* **2004**, *84*, 4233–4235. [[CrossRef](#)]
28. Wu, J.-J.; Liu, S.-C.; Yang, M.-H. Room-temperature ferromagnetism in well-aligned Zn<sub>1-x</sub>Co<sub>x</sub>O nanorods. *Appl. Phys. Lett.* **2004**, *85*, 1027–1029. [[CrossRef](#)]
29. Knut, R.; Wikberg, J.M.; Lashgari, K.; Coleman, V.A.; Westin, G.; Svedlindh, P.; Karis, O. Magnetic and electronic characterization of highly Co-doped ZnO: An annealing study at the solubility limit. *Phys. Rev. B* **2010**, *82*, 094438. [[CrossRef](#)]
30. Vijayalakshmi, S.; Venkataraj, S.; Jayavel, R. Characterization of cadmium doped zinc oxide (Cd: ZnO) thin films prepared by spray pyrolysis method. *J. Phys. D Appl. Phys.* **2008**, *41*, 245403. [[CrossRef](#)]
31. Munõz, E.L.; Mercurio, M.E.; Cordeiro, M.R.; Pereira, L.F.D.; Carbonari, A.W. Rentería, M. Dynamic hyperfine interactions in <sup>111</sup>In/<sup>111</sup>Cd-doped ZnO semiconductor: PAC results supported by Ab initio calculations. *Phys. B Condens. Matter* **2012**, *407*, 3121–3124. [[CrossRef](#)]
32. Uddin, J.; Scuseria, G.E. Theoretical study of ZnO phases using a screened hybrid density functional. *Phys. Rev. B* **2006**, *74*, 245115. [[CrossRef](#)]
33. Jaffe, J.E.; Snyder, J.A.; Lin, Z.; Hess, A.C. LDA and GGA calculations for high-pressure phase transitions in ZnO and MgO. *Phys. Rev. B* **2000**, *62*, 1660. [[CrossRef](#)]
34. Hu, S.-J.; Yan, S.-S.; Zhao, M.-W.; Mei, L.-M. First-principles LDA+U calculations of the Co-doped ZnO magnetic semiconductor. *Phys. Rev. B* **2006**, *73*, 245205. [[CrossRef](#)]
35. Chanier, T.; Sargolzaei, M.; Opahle, I.; Hayn, R.; Koepf, K. LSDA+U versus LSDA: Towards a better description of the magnetic nearest-neighbor exchange coupling in Co- and Mn-doped ZnO. *Phys. Rev. B* **2006**, *73*, 134418. [[CrossRef](#)]
36. Sato, K.; Katayama-Yoshida, H. First principles materials design for semiconductor spintronics. *Semicond. Sci. Technol.* **2002**, *17*, 367. [[CrossRef](#)]
37. Pechini, M.P. Method of Preparing Lead and Alkaline Earth Titanates and Niobates and Coating Method Using the Same to Form a Capacitor. U.S. Patent US3330967A, 11 July 1967.
38. Haas, H.; Röder, J.; Correia, J.G.; Schell, J.; Fenta, A.S.; Vianden, R.; Larsen, E.M.H.; Aggelund, P.A.; Fromsejer, R.; Hemmingsen, L.B.S.; et al. Free Molecule Studies by Perturbed  $\gamma - \gamma$  Angular Correlation: A New Path to Accurate Nuclear Quadrupole Moments. *Phys. Rev. Lett.* **2021**, *126*, 103001. [[CrossRef](#)] [[PubMed](#)]
39. Schatz, G.; Weidinger, A. *Nuclear Condensed Matter Physics. Nuclear Methods and Applications*; Wiley and Sons: Chichester, UK, 1996.
40. Abragam, A.; Pound, R.V. Influence of electric and magnetic fields on angular correlations. *Phys. Rev.* **1953**, *92*, 943. [[CrossRef](#)]
41. Carbonari, A.W.; Mestnik-Filho, J.; Saxena, R.N. Impurities in Magnetic Materials Studied by PAC Spectroscopy. *Defect Diffus. Forum* **2011**, *311*, 39. [[CrossRef](#)]
42. Kokalj, A. XCrySDen—A new program for displaying crystalline structures and electron densities. *J. Mol. Graph. Model.* **1999**, *17*, 176–179. [[CrossRef](#)]
43. Andersen, O.K. Linear methods in band theory. *Phys. Rev. B* **1975**, *12*, 3060. [[CrossRef](#)]
44. Blaha, P.; Schwarz, K.; Madsen, G.K.H.; Kvasnicka, D.; Luitz, J.; Laskowski, R.; Tran, F.; Marks, L.D. *WIEN2k: An Augmented Plane Wave+ Local Orbitals Program for Calculating Crystal Properties*; Vienna University of Technology: Vienna, Austria, 2018.
45. Perdew, J.P.; Burke, K.; Ernzerhof, M. Generalized gradient approximation made simple. *Phys. Rev. Lett.* **1996**, *77*, 3865. [[CrossRef](#)] [[PubMed](#)]
46. Wu, Z.; Cohen, R.E. More accurate generalized gradient approximation for solids. *Phys. Rev. B* **2006**, *73*, 235116. [[CrossRef](#)]
47. Albertsson, J.; Abrahams, S.C.; Kvick, Å. Atomic displacement, anharmonic thermal vibration, expansivity and pyroelectric coefficient thermal dependences in ZnO. *Acta Crystallogr. Sect. B Struct. Sci.* **1989**, *45*, 34–40. [[CrossRef](#)]
48. Blaha, P.; Schwarz, K.; Herzig, P. First-principles calculation of the electric field gradient of Li<sub>3</sub>N. *Phys. Rev. Lett.* **1985**, *54*, 1192. [[CrossRef](#)] [[PubMed](#)]
49. Inglot, Z.; Wegner, D. Perturbed angular correlation measurements of <sup>111</sup>Cd in cobalt (II, III) oxide. *J. Phys. Condens. Matter* **1991**, *3*, 2137. [[CrossRef](#)]

50. Kumar, S.; Basu, S.; Rana, B.; Barman, A.; Chatterjee, S.; Jha, S.N.; Bhattacharyya, D.; Sahoo, N.K.; Ghosh, A.K. Structural, optical and magnetic properties of sol–gel derived ZnO: Co diluted magnetic semiconductor nanocrystals: An EXAFS study. *J. Mater. Chem. C* **2014**, *2*, 481–495. [[CrossRef](#)]
51. Shannon, R.D. Revised effective ionic radii and systematic studies of interatomic distances in halides and chalcogenides. *Acta Crystallogr. Sect. A Cryst. Phys. Diffr. Theor. Gen. Crystallogr.* **1976**, *32*, 751–767. [[CrossRef](#)]
52. Mesquita, A.; Rhodes, F.P.; da Silva, R.T.; Neves, P.P.; De Zevallos, A.O.; Andreetta, M.R.B.; de Lima, M.M., Jr.; Cantarero, A.; Da Silva, I.S.; Boselli, M.A.; et al. Dynamics of the incorporation of Co into the wurtzite ZnO matrix and its magnetic properties. *J. Alloys Compd.* **2015**, *637*, 407. [[CrossRef](#)]
53. Yadav, M.; Ghosh, M.; Biswas, R.; Raychaudhuri, A.; Mookerjee, A.; Datta, S. Band-gap variation in Mg- and Cd-doped ZnO nanostructures and molecular clusters. *Phys. Rev. B* **2007**, *76*, 195450. [[CrossRef](#)]
54. Jule, L.T.; Dejene, F.B.; Ali, A.G.; Roro, K.T.; Hegazy, A.; Allam, N.K.; El Shenawy, E. Wide visible emission and narrowing band gap in Cd-doped ZnO nanopowders synthesized via sol-gel route. *J. Alloys Compd.* **2016**, *687*, 920–926. [[CrossRef](#)]
55. Palacios, P.; Aguilera, I.; Wahnón, P. Electronic structure and optical properties in ZnO: M (Co, Cd): Effect of band-gap variation. *Thin Solid Film.* **2010**, *518*, 4568–4571. [[CrossRef](#)]
56. Bredow, T.; Gerson, A.R. Effect of exchange and correlation on bulk properties of MgO, NiO, and CoO. *Phys. Rev. B* **2000**, *61*, 5194. [[CrossRef](#)]
57. Sato, K.S.K.; Katayama-Yoshida, H.K.-Y.H. Material design for transparent ferromagnets with ZnO-based magnetic semiconductors. *Jpn. J. Appl. Phys.* **2000**, *39*, L555. [[CrossRef](#)]
58. Dietl, T.; Ohno, H.; Matsukura, F.; Cibert, J.; Ferrand, D. Zener model description of ferromagnetism in zinc-blende magnetic semiconductors. *Science* **2000**, *287*, 1019–1022. [[CrossRef](#)] [[PubMed](#)]
59. Ng, H.T.; Chen, B.; Li, J.; Han, J.; Meyyappan, M.; Wu, J.; Li, S.X.; Haller, E.E. Optical properties of single-crystalline ZnO nanowires on m-sapphire. *Appl. Phys. Lett.* **2003**, *82*, 2023–2025. [[CrossRef](#)]
60. Chiorescu, C.; Cohn, J.L.; Neumeier, J.J. Impurity conduction and magnetic polarons in antiferromagnetic oxides. *Phys. Rev. B* **2007**, *76*, 020404. [[CrossRef](#)]
61. Shatnawi, M.; Alsmadi, A.M.; Bsoul, I.; Salameh, B.; Alna'Washi, G.A.; Al-Dwari, F.; El Akkad, F. Magnetic and optical properties of Co-doped ZnO nanocrystalline particles. *J. Alloys Compd.* **2016**, *655*, 244–252. [[CrossRef](#)]
62. Darriba, G.N.; Errico, L.A.; Eversheim, P.D.; Fabricius, G.; Rentería, M. First-principles and time-differential  $\gamma - \gamma$  perturbed-angular-correlation spectroscopy study of structural and electronic properties of Ta-doped TiO<sub>2</sub> semiconductor. *Phys. Rev. B* **2009**, *79*, 115–213. [[CrossRef](#)]
63. Darriba, G.N.; Muñoz, E.L.; Carbonari, A.W.; Rentería, M. Experimental TDPAC and theoretical DFT study of structural, electronic, and hyperfine properties in (<sup>111</sup>In→) <sup>111</sup>Cd-doped SnO<sub>2</sub> semiconductor: Ab initio modeling of the electron-capture-decay after-effects phenomenon. *J. Phys. Chem. C* **2018**, *122*, 17423–17436. [[CrossRef](#)]
64. Oliveira, G.N.P.; Teixeira, R.C.; Moreira, R.P.; Correia, J.G.; Araújo, J.P.; Lopes, A.M.L. Local inhomogeneous state in multiferroic SmCrO<sub>3</sub>. *Sci. Rep.* **2020**, *10*, 46–86. [[CrossRef](#)]

**Disclaimer/Publisher's Note:** The statements, opinions and data contained in all publications are solely those of the individual author(s) and contributor(s) and not of MDPI and/or the editor(s). MDPI and/or the editor(s) disclaim responsibility for any injury to people or property resulting from any ideas, methods, instructions or products referred to in the content.